An Overview of the AIRS Radiative Transfer Model

L. Larrabee Strow, Scott E. Hannon, Sergio De Souza-Machado, Howard E. Motteler, *Member, IEEE*, and David Tobin

Abstract—The two main elements of the Atmospheric Infrared Sounder Radiative Transfer Algorithm (AIRS-RTA) are described in this paper: 1) the fast parameterization of the atmospheric transmittances that are used to perform the AIRS physical retrievals and 2) the spectroscopy used to generate the parameterized transmittances. We concentrate on those aspects of the spectroscopy that are especially relevant for temperature and water vapor retrievals. The AIRS-RTA is a hybrid model in that it parameterizes most gases on a fixed grid of pressures, while the water optical depths are parameterized on a fixed grid of water amounts. Water vapor, ozone, carbon monoxide, and methane profiles can be varied, in addition to the column abundance of carbon dioxide.

Index Terms—Atmospheric retrievals, radiative transfer, remote sensing, spectroscopy.

I. INTRODUCTION

THE ATMOSPHERIC Infrared Sounder (AIRS) [1] uses a physical algorithm for the retrieval of atmospheric profiles, and consequently is dependent on an accurate, and fast, radiative transfer algorithm for computing clear-air radiances. The AIRS physical retrieval algorithm uses approximately 300 channels to determine temperature, water, and ozone profiles. Additional channels are used to retrieve methane, carbon monoxide, and eventually carbon dioxide. Calls to the atmospheric infrared sounder radiative transfer algorithm (AIRS-RTA) represent the most CPU-intensive part of the operational processing, so the RTA must be fast. The high spectral resolution of AIRS coupled with its low noise should produce retrievals that are as good, or better, than the worldwide operational radiosonde network, if the forward model accuracy approaches the noise level of the instrument.

Two primary components of the AIRS-RTA determine its accuracy: 1) the spectroscopy used to compute atmospheric transmittances and 2) the quality of the fast model transmittance parameterization. We review here the basic form of the AIRS-RTA parameterization and its accuracy. A detailed explanation of the procedures used to generate the parameterization coefficients is beyond the scope of the paper.

We will also review the spectroscopy used to generate the AIRS-RTA parameterization and the associated line-by-line

(LBL) algorithms that generate the monochromatic transmittances required for producing the fast radiative transfer model. This discussion focuses on the characteristics that distinguish our LBL algorithms from others and will include comparisons between up-welling atmospheric radiances observed with high-spectral resolution radiometers flying on the National Aeronautics and Space Administration's (NASA) ER-2 aircraft and radiances computed using our LBL algorithm.

See [1] for an overview of the AIRS instrument and [3] for details on the AIRS spectral resolution and spectral response functions (SRFs). AIRS design parameters relevant for the radiative transfer algorithm are 1) a 650-cm^{-1} (15 μm) to 2700-cm^{-1} (3.7 μm) spectral range with 2378 channels; 2) SRFs with full widths at half maximum of $\sim\nu/1200$ (0.5–2.3 cm^{-1}); and 3) noise levels on the order of 0.2 K (70% of AIRS channels have noise less than 0.2 K, 20% have noise less then 0.1 K).

II. RADIATIVE TRANSFER

The observed AIRS radiance for channel i is the integrated product ("convolution") of the monochromatic radiance R_ν with the normalized instrument SRF for channel i

$$R_i^{\mathrm{obs}} = \int_{\Delta\nu_i} R_\nu \, \mathrm{SRF}_i(\nu) \, d\nu. \tag{1}$$

The retrieval of atmospheric parameters from R^{obs} is accomplished by varying an initial guess for the temperature $T(p)$ and constituent amounts until the difference between observed and calculated radiances is minimized for some selection of channels i.

The monochromatic radiance leaving the top of a nonscattering, clear atmosphere is

$$R_\nu = \epsilon_\nu B_\nu(T_s)\tau_\nu(p_s \to 0, \theta_{\mathrm{sat}})$$
$$+ \int_{p_s}^{0} B_\nu(T(p)) \frac{d\tau_\nu(p \to 0, \theta_{\mathrm{sat}})}{dp} \, dp$$
$$+ F_\nu^d \rho_\nu^t \tau_\nu(p_s \to 0, \theta_{\mathrm{sat}})$$
$$+ \frac{H_\nu}{\sec(\theta_{\mathrm{sun}})} \tau_\nu(0 \to p_s, \theta_{\mathrm{sun}})\rho_\nu^s\tau_\nu(p_s \to 0, \theta_{\mathrm{sat}}). \tag{2}$$

The first term is the surface blackbody emission where ϵ_ν is the surface emissivity and $B_\nu(T_s)$ is the Planck function. The second term is the atmospheric emission, followed by the down-welling atmospheric emission reflected by the surface. F_ν^d is the down-welling thermal flux and ρ_ν^t the reflectance of this flux by the surface, which we assume to be Lambertian. Reflected solar radiation is represented by the last term in this equation, where H_ν is the solar irradiance incident at the top of the atmosphere

and ρ_ν^s is the solar reflectance by the surface. All of these terms involve the atmospheric layer-to-space transmittance from some pressure p to space at angle θ_{sat}, the satellite zenith angle as measured along the ray from the surface to the satellite

$$\tau_\nu(p \to 0, \theta_{\text{sat}}) = \prod_g \exp\left[-\int_p^0 k_\nu^g(p, \theta_{\text{sat}})\, dp\right] \quad (3)$$

where $k_\nu^g(p, \theta_{\text{sat}})$ is the optical depth per unit pressure for the gas g at pressure p viewed at angle θ_{sat}. Note that the τ_ν also depends on $T(p)$ and the abundance of the radiatively active atmospheric constituents, although this is not shown explicitly.

We can simplify the solar contribution by noting that the two solar transmittances in (2) can be combined into a single, longer path transmittance

$$\tau_\nu(p_s \to 0, \theta_{\text{eff}}) = \tau_\nu(0 \to p_s, \theta_{\text{sun}})\tau_\nu(p_s \to 0, \theta_{\text{sat}}) \quad (4)$$

where

$$\theta_{\text{eff}} = \sec^{-1}\left(\sec(\theta_{\text{sun}}) + \sec(\theta_{\text{sat}})\right). \quad (5)$$

A. Channel-Averaged Radiative Transfer

The AIRS forward model uses a discretized version of (2) for each spectral channel i

$$R^i = \epsilon_\nu B_\nu(T_s)\mathcal{T}_s^i(\theta_{\text{sat}}) + \sum_{l=1}^{l_s} B_\nu(T_l)(\mathcal{T}_{l-1}^i(\theta_{\text{sat}}) - \mathcal{T}_l^i(\theta_{\text{sat}}))$$
$$+ R_{\text{refl. th.}}^i + H_\nu \cos(\theta_{\text{sun}})\rho_\nu^s \mathcal{T}_s^i(\theta_{\text{eff}}) \quad (6)$$

with 100 atmospheric layers l, which is sufficiently fine to keep discretization errors below the AIRS noise level. l_s is the first atmospheric layer above the surface, which in practice is generally some fraction of one of the 100 fixed pressure layers.

The channel-averaged layer-to-space transmittances in this equation are given by

$$\mathcal{T}_l^i(\theta) \equiv \int_{\Delta\nu_i} \tau_\nu(p_l \to 0, \theta)\text{SRF}_i(\nu)\, d\nu. \quad (7)$$

AIRS channels are narrow enough that we can replace the convolution of the Planck function with its value at channel center, which introduces errors below the 0.1 K level. The solar irradiance term is the convolution of the AIRS SRF with a solar spectrum derived from the Atmospheric Trace Molecule Spectroscopy (ATMOS) experiment [4]. The channel-averaged version of the reflected thermal term, $R_{\text{refl. th.}}$ will be discussed later.

The parameterization of the gas transmittances is quite involved, and will be simplified in this discussion by assuming that the algorithm only needs to vary water and ozone transmittances as a function of gas amount, observation secant angle, and temperature. This leaves us with three separate transmittance terms; one for all gases with fixed amounts, including CO_2, that we label $g = F$, one for water vapor transmittances labeled $g = W$, and one for ozone labeled $g = O$. The AIRS radiative transfer algorithm can also vary methane and carbon monoxide profiles, and adjust the total column of CO_2. Since Beer's law

is not obeyed for convolved transmittances we cannot directly compute the total convolved transmittance in (7) as the product of the individual convolved transmittances, since

$$\mathcal{T}_l \equiv \mathcal{T}_l^{FWO} \neq \mathcal{T}_l^F \mathcal{T}_l^W \mathcal{T}_l^O \quad (8)$$

where

$$\mathcal{T}_l^g(\theta) = \int_{\Delta\nu} \tau_\nu^g(p_l \to 0, \theta)\text{SRF}(\nu)\, d\nu. \quad (9)$$

Recovery of Beer's law is partially possible by expressing the individual convolved transmittances in the following way as suggested by Susskind [5]

$$\mathcal{T}_l^{W,\,\text{eff}} = \frac{\mathcal{T}_l^{FW}}{\mathcal{T}_l^F} \quad \text{and} \quad \mathcal{T}_l^{O,\,\text{eff}} = \frac{\mathcal{T}_l^{FWO}}{\mathcal{T}_l^{FW}}. \quad (10)$$

Using these definitions for the individual convolved transmittances we see in the following equation that we recover the true total convolved transmittance after multiplication

$$\mathcal{T}_l^{\text{eff}} = \mathcal{T}_l^F \mathcal{T}_l^{W,\,\text{eff}} \mathcal{T}_l^{O,\,\text{eff}} = \mathcal{T}_l^F \frac{\mathcal{T}_l^{FW}}{\mathcal{T}_l^F} \frac{\mathcal{T}_l^{FWO}}{\mathcal{T}_l^{FW}} = \mathcal{T}_l^{FWO}. \quad (11)$$

The aforementioned relation is only correct if the $\mathcal{T}_l^{g,\,\text{eff}}$ can be accurately parameterized as a function of the atmospheric temperature and gas profile, and with satellite viewing angle. The parameterization accuracy is increased if the most dominant gas transmittance for a given channel is formed alone, as was done for $\mathcal{T}_l^{F,\,\text{eff}}$ in (11). Additional details on how the carbon monoxide and methane transmittances are handled are discussed in [2].

Since the layer optical depth $k_l^{g,\,\text{eff}}$ has a more linear dependence on temperature and gas abundance than the transmittance, we parameterize the layer optical depths, which are easily formed from the layer-to-space transmittances

$$k_l^{g,\,\text{eff}} = -\ln\left[\frac{\mathcal{T}_l^{g,\,\text{eff}}}{\mathcal{T}_{l-1}^{g,\,\text{eff}}}\right]. \quad (12)$$

Most optical depths are linearly parameterized (see Section II-C for exceptions) as

$$k_l^{g,\,\text{eff}} = \sum_j c_j^{g,\,l} Q_j \quad (13)$$

where the constant terms $c_j^{g,\,l}$ are determined from least squares regression of the above equation to a statistical set of atmospheric profiles. The predictors, Q_j, and regression techniques are discussed in more detail later. The final form of the AIRS radiative transfer equation uses $\mathcal{T}_l^{\text{eff}}$, as shown below, for $\mathcal{T}_l^i(\theta_{\text{sat}})$ in (6)

$$\mathcal{T}_l^{\text{eff}} = \prod_g \prod_{l'=1}^{l} \exp\left(-\sum_j c_j^{g,\,l} Q_j\right). \quad (14)$$

Similar, but more complicated procedures are used to develop transmittance equations for the other variable gases, carbon monoxide, and methane. Variable CO_2 is treated as a special case; see Section II-F.

B. Reflected Down-Welling Thermal Radiance

The down-welling thermal flux reflected by the surface is generally a small but not negligible term that will increase observed brightness temperatures by nominally 0.2 K for $\epsilon = 0.98$. This term can grow to ~ 0.6 K in regions of low emissivity, such as over silicate deserts.

The monochromatic down-welling thermal flux (for a clear nonscattering atmosphere) can be accurately computed using the standard diffusivity approximation (Goody and Yung)

$$F_\nu^d = \pi \sum_{l=1}^{l_s} B_\nu(T_l)[\tau_\nu(p_{l+1} \to p_s, \theta_{d,l+1}) \\ -\tau_\nu(p_l \to p_s, \theta_{d,1})] \quad (15)$$

where $\theta_{d,1}$ is the diffusivity angle for layer l. The $R_{\text{refl. th.}}$ term in the discretized version of the radiative transfer equation (before convolution with the SRFs) is, therefore

$$R_{\text{refl. th.}} = \pi \rho_\nu^t \tau_\nu(p_s \to 0, \theta_{\text{sat}}) \sum_{l=1}^{l_s} B_\nu(T_l) \\ \cdot [\tau_\nu(p_{l+1} \to p_s, \theta_{d,l+1}) - \tau_\nu(p_l \to p_s, \theta_{d,1})]. \quad (16)$$

We partially rewrite this equation in terms of the layer transmittance $\tilde{\tau}_\nu(p_l, \theta_{d,1})$

$$R_{\text{refl. th.}} = \pi \rho_\nu^t \tau_\nu(p_s \to 0, \theta_{\text{sat}}) \sum_{l=1}^{l_s} B_\nu(T_l) \\ \cdot [1 - \tilde{\tau}_\nu(p_l, \theta_{d,1})]\tau_\nu(p_{l+1} \to p_s, \theta_{d,l+1}) \quad (17)$$

in order to clarify the following approximation to this relation.

Even within the diffusivity approximation the exact computation of the above quantity takes significant time, since it requires transmittances at different angles than the direct emission term. Moreover, since this term is quite small, significant approximations may be warranted. Since most of the down-welling flux that ultimately is reflected back to the satellite is coming from the lower troposphere, Kornfield and Susskind [6] suggested modeling the down-welling flux as emission from a single atmospheric layer with temperature T_i as

$$R_{\text{i, refl. th.}}^{\text{eff}} = \pi \rho_\nu^t \mathcal{T}_s^i(\theta_{\text{sat}})B(T_i)(1 - \mathcal{T}_s^i(\theta_{\text{sat}}))F^i \quad (18)$$

where F^i is a correction factor determined using regression over a statistical set of profiles. Note, we are using channel convolved values for the transmittances in the above equation. A different layer temperature T_i is used for each channel by finding which layer resulted in the most accurate approximation for this radiance term. F_i was modeled as a linear equation with five predictors; a constant, $1/a$, $B(T_i)$, $B(T_i)/a$, and $B(T_s)/B(T_i)$, where a is the secant of θ_{sat}. Note that this approximation for the reflected thermal radiation only uses transmittances that are already computed for the larger atmospheric emission radiance term. We estimate that this approximation for reflected thermal radiation is accurate on average to $\sim 15\%$ to 20%. In the future we may find that this term requires further improvements.
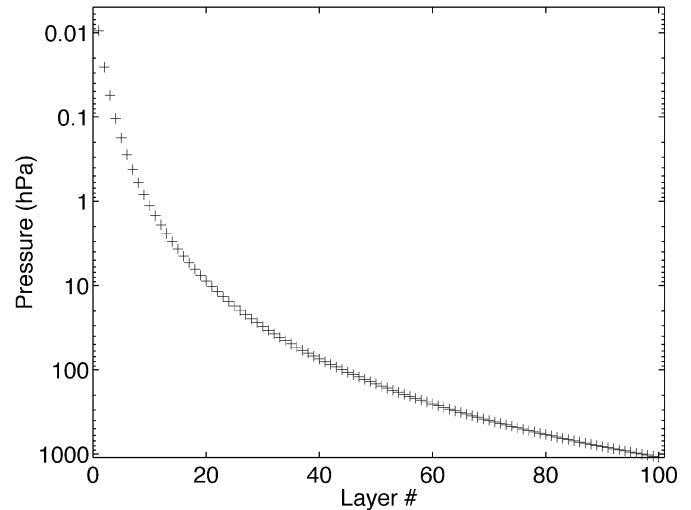

Fig. 1. Mean layer pressures used in the AIRS fast radiative transfer model.

C. Atmospheric Layering

The AIRS fast model uses two different layering methods to model the optical depths. The most intuitive is a grid of vertical slabs with constant pressure. In this case, each layer is defined by the two bounding grid pressure levels (so N layers require a $N+1$ level grid). The discretized version of the radiative transfer equation discussed in the previous section uses this 100-layer pressure grid and ultimately all T_ls must be available on this grid. All component gas transmittances, with the exception of water vapor for ~ 600 channels, are parameterized on this grid which spans the range 1100–0.005 hPa. The 101 atmospheric pressure *levels* which divide the atmosphere into 100 layers are defined as

$$P_{\text{lev}}(i) = (Ai^2 + Bi + C)^{7/2} \quad (19)$$

where i is level number, and A, B, and C are constants. By fixing $P_{\text{lev}}(1) = 1100$, $P_{\text{lev}}(38) = 300$, and $P_{\text{lev}}(101) = 0.005$ hPa, we can then solve for these three constants. This relation gives us smoothly varying layers and is fine enough to not limit the accuracy of the radiative transfer equation. A plot of these layers is shown in Fig. 1. Note that although the level numbering has level 1 closest to the surface, the layer numbering scheme used in the AIRS-RTA has layer 1 closest to the satellite.

A second method for layering the atmosphere (introduced in [7] and [8]) called OPTRAN is used for ~ 600 channels that are dominated by water vapor. Water vapor amounts can vary by three orders of magnitude in the lower troposphere, producing high variability in the transmittances that are difficult to parameterize accurately. OPTRAN interpolates the atmospheric profile under consideration onto a grid of layers that have constant layer-to-space water amounts. The optical depth is computed on this grid and then interpolated back to the constant pressure grid for performing radiative transfer. The main predictor for optical depth on the OPTRAN grid is pressure, rather than a combination of secant angle and gas amount, as is the case on a constant pressure grid. In order to achieve acceptable accuracies with OPTRAN we used 300 grid layers of constant water amount.

Although OPTRAN produces more accurate parameterization using a smaller number of parameters for most water vapor channels, we found that a grid of constant pressure layers worked better for the fixed gas transmittances [9]. Consequently, the AIRS transmittance parameterization is a hybrid of both methods.

D. Predictors

The layer effective optical depths are modeled as simple functions of various profile-dependent predictors [the terms Q_i in (14)]. Typically these predictors are terms related to the layer temperature, absorber amount, and viewing angle, and for OPTRAN, pressure. However, the loss of Beer's law means that the functional dependence of the transmittances on the predictors can be quite complex, so the exact selection of predictors involves a combination of insight and trial-and-error testing. In addition, the layer optical depths also depend on the layers above them (at higher altitudes), which is a natural consequence of deriving the layer effective optical depths from ratios of layer-to-space transmittances.

A detailed discussion of all predictors used for all channels and gases is beyond the scope of this paper, so instead we summarize the profile variables that make up the actual predictors.

The predictors are products of various powers of the following profile variables; a the secant of the path zenith angle, $T_r = T_l/T_l^{\text{ref}}$, $\Delta T = T_l - T_l^{\text{ref}}$, ratios of the various gas amounts (water, ozone, methane, carbon monoxide) to their reference values, and some additional variables that are nonlocal in that they depend on the profile above the layer under consideration. The gas amounts refer to the amount of the absorber contained within the layer along a nadir path. To insure that the predictors are of the same magnitude most are ratioed or differenced with a layer temperature or amount from a reference profile (U.S. Standard Atmosphere). For example, two predictor variables that take into account the dependence of the layer transmittances on the layers above are

$$T_z = \sum_{i=2}^{L} P(l)\,(P(l) - P(l-1))\,T_r(l-1) \qquad (20)$$

and

$$W_z = \frac{\sum\limits_{i=1}^{L} P(l)\,((P(l) - P(l-1))\,W_{\text{prof}}(l)}{\sum\limits_{i=1}^{L} P(l)\,((P(l) - P(l-1))\,W_{\text{ref}}(l)} \qquad (21)$$

where $P(l)$ is the pressure, $W_{\text{prof}}(l)$ the profile water amount, and $W_{\text{ref}}(l)$ the water amount for the reference profile. Similar variables to W_z for ozone, carbon monoxide, and methane are also used.

We used 11 temperature predictors in (14) that were constructed from various products of powers of a, T_r, and T_z. For water vapor optical depths the predictors include up to 13 products of powers of a, W, W_z, ΔT, and two variables similar to W_z but for ozone and methane. Ozone used a maximum of ten products of various powers of a, O, ΔT, and T_o. CO and CH$_4$ optical depths each used up to ten products of four predictors analogous to those used for O_3. The water vapor continuum

was parameterized with products of powers of a, W, and T_r. Finally, the CO$_2$ column content was parameterized with four products of powers of a and T_r. The exact selection of predictors are available in [10]. The resulting coefficients for all 2378 channels, 100 layers, and four variable gases requires 35 MB of storage.

Since the OPTRAN layering scheme uses a grid of constant layer-to-space water amounts while AIRS radiative transfer is on a constant pressure grid, we calculate the OPTRAN predictors at the AIRS pressure layers and then linearly interpolate them to the OPTRAN grid. We used nine predictors for OPTRAN; a constant, P_l, T_l, $\sqrt{(P_l)}$, T_l^2, $P_l T_l$, a_l, P_{zl}, and T_{zl}, where

$$P_{zl} = \frac{\sum\limits_{i=l}^{1} P(l)\,a(l)\,W(l)}{\sum\limits_{i=l}^{1} a(l)\,W(l)} \qquad (22)$$

and

$$T_{zl} = \frac{\sum\limits_{i=l}^{1} T_l\,a(l)\,W(l)}{\sum\limits_{i=l}^{1} a(l)\,W(l)}. \qquad (23)$$

Once these predictors are interpolated onto the OPTRAN grid they are normalized by dividing them by a reference profile (also interpolated to the OPTRAN grid) to keep all predictor values close to unity.

E. Regressions

The successful determination of the fast model parameterization coefficients is highly dependent on weighting the various terms in the regression equation (14). Recall that the atmospheric emission from a single layer is proportional to the product $(1 - \tilde{\tau})\tau$ where $\tilde{\tau}$ is a layer transmittance and τ is a layer-to-space transmittance. We can define a transmittance error as

$$\Delta \tau_{\text{error}} = \exp(-k) - \exp(-k * (1 + \epsilon)) \qquad (24)$$

where k is the optical depth and ϵ represents some small fractional error in k. A plot of this equation resembles the shape of the curve shown in Fig. 2. The transmittance is most sensitive to optical depths near unity, and insensitive to small or large optical depths.

Consequently, during the regressions to determine the fast model coefficients we adjust the input optical depth to arrive at the weighted values shown in Fig. 2, except that we limit the minimum weighted k to one. The final k_{weighted} used in the regression is the product of the weighted values determined separately for the layer optical depth and for the layer-to-space optical depth. To maintain the balance of (13), we must apply the same weighting factor $k_{\text{weighted}}/k_{\text{initial}}$ to the predictors.

The regression training dataset consists of 48 profiles, each calculated at six viewing angles between nadir and 60°. The 48 profiles were selected to span the expected range of profile variability and were mostly selected from the TIGR [11] profile database. Data for an additional six angles extending out to 83°
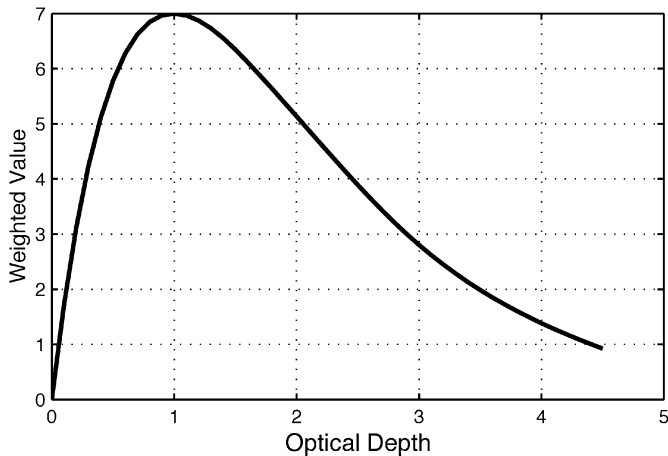
Fig. 2. Weighted values used for optical depths used in regressions for fast model parameters.

was created for the shortwave channels because of the longer pathlengths that arise in the reflected solar term of the radiative transfer equation. Care should be taken in using the AIRS-RTA at large solar zenith angles due to uncertainties in the true atmospheric path under those conditions.

The monochromatic transmittances for each profile were calculated using the KCARTA [12], [13] code, and included all gases contained in the 1996/1998 HITRAN [14] database (HITRAN 2000, Version 11.0 will be used in the near future). Profiles for the minor gases that do not vary in the fast radiative transfer model were set to climatological mean values.

The water vapor continuum was parameterized separately from the line spectra, since it is essentially constant over the width of an AIRS channel and can be removed from the instrument convolution. This also makes it easier to parameterize the water line spectra. In addition, it allows us to modify the water continuum in the AIRS fast model separately from the contributions to the water transmittances due to the line spectra. This has the practical advantage that we can easily modify the continuum, which is the more uncertain part of the spectrum.

To simplify the fast model, the "fixed" gas amounts were kept identical in all the regression profiles, and only the layer temperatures were allowed to vary. Small variations in layer gas amount caused by the combined effects of water vapor displacement, gravity (as a function of latitude), and layer pathlength (required to keep the layer pressure constant) are typically less than 1% to 2%. We have parameterized these effects with a term we call the "G-factor" that modifies the fixed gas optical depth $k_l^{F, \text{eff}}$.

The regression profiles are also used to compute the reflected down-welling thermal radiance using kCARTA, generating the dataset needed to determine T_i and F^i in (18).

F. Variable CO_2

The at-launch AIRS radiative transfer algorithm allows variation of the CO_2 column amount although this capability is not presently used in the AIRS retrieval algorithm. Climatological (hemispherical and seasonal) variations in CO_2 mixing ratio of a few parts per million volume (ppmv) are large enough to observe with AIRS, so we need the capability to compute the ef-

fects of CO_2 on AIRS radiances when analyzing biases. In the long term the potential for AIRS to retrieve CO_2 will be carefully examined.

CO_2 should only vary globally by several percent at most, resulting in changes to the optical depth that are very linear in CO_2 amount. For simplicity we treat CO_2 as one of the "fixed" gases and model the small variability of CO_2 as a separate additive perturbation term as follows:

$$\Delta k_l^{\text{eff}} = \delta \, CO_2(\%) \sum_{j=1}^{4} d_j^l Q_j \qquad (25)$$

where the d_j^l are constant coefficients determined by regression, and the predictors Q_j are a, T_r, aT_r, and $a(T_r)^2$. $\delta \, CO_2(\%)$ is the percentage increase or decrease in the CO_2 mixing ratio from our standard value of 370 ppmv. The regression for the d_j^l constants requires computing convolved monochromatic transmittances with our standard value for the CO_2 and with an enhanced CO_2 mixing ratio.

Note that we only vary the CO_2 in the regression profiles by a constant ppmv offset in every layer. This means that, in principle, $\delta \, CO_2(\%)$ in (25) should be the same for all layers l. Our parameterization for variable CO_2 is very accurate, far below the AIRS noise levels. Consequently, we expect that one could vary the CO_2 profile (and not just the column) to some degree and not introduce significant errors, although we have not carefully evaluated any potential errors that could arise under these conditions.

This correction to the fixed gas optical depths for variable CO_2 will generally have the same order of magnitude as the G-factor correction discussed in the previous section. The G-factor correction modifies the amount of fixed gases (including CO_2) in a layer to account for displacement by highly variable water vapor, which must be done to keep the layer pressure constant. However, note that the G-factor correction is applied to all channels, not just those with water vapor emission, and thus must be done accurately in order to retrieve variable CO_2.

G. Accuracy and Performance

Fig. 3 shows the fitting errors, in brightness temperature units, for the fast transmittance regressions (middle panel). This plot does not include errors that may be introduced by the reflected thermal parameterization, which are highly dependent on the surface reflectivity. The bottom panel of Fig. 3 shows brightness temperature errors of the AIRS-RTA when using an independent dataset, which was a selection of 212 profiles from the TIGR dataset that were not used as fitting profiles. These 212 profiles were selected to evenly cover the globe to the extent possible with TIGR.

Histograms of the fast model parameterization errors for both the dependent and independent profile dataset shown in Fig. 4 show that the vast majority of channels have errors below 0.1 K. For clarity we truncated the histogram x axis a little above 0.2 K, which removes two/four channels from the histogram for the dependent/independent profile sets, respectively. Errors are larger for the independent profile set, mostly for channels in regions dominated by water that had extremely low fitting errors. On
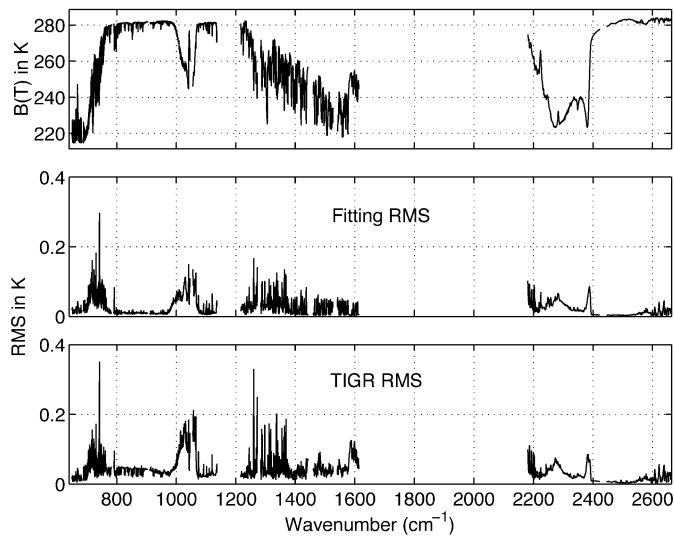
Fig. 3. (Top) A simulated AIRS spectrum. (Middle) RMS difference between fast model $B(T)$ and true $B(T)$ for the 48 regression profiles, for five slant paths. (Bottom) Same as middle, but using 212 independent profiles from the TIGR database.

Fig. 4. Distribution of fitting errors in the AIRS-RTA.

average the mean rms error increased by about 50% to 0.04 K with the independent profile set. If our profile statistics are representative, spectroscopy errors (and in a few cases SRF uncertainties) rather than parameterization errors should dominate the uncertainties in the AIRS-RTA.

The largest errors in the fast model parameterization are for two to three high-altitude CO_2 channels that have interfering water vapor lines. These channels are easily avoided in the retrieval, since there are sufficient numbers of high-altitude CO_2 channels that do not have water vapor interference. The AIRS-RTA parameterization errors are also higher than average for a subset of water channels centered on water vapor lines of medium strength in the 1250–1375-cm^{-1} region. These channels are generally avoided in the retrieval because they have broader weighting functions than channels located in-between spectral lines that peak at the same altitude.

The AIRS-RTA integrates the radiative transfer equation using the 100-layer model of the atmosphere. However, the AIRS physical retrieval algorithm methodology does not require evaluation of *radiance* derivatives for each of the 100 layers (see [15, Table 1]). Temperature retrievals, for example, use 24 vertical temperature derivatives of the radiance, corresponding to the 24 trapezoid functions discussed in [15]. This approach significantly lowers the CPU requirements on the RTA and allows the use of finite difference radiance derivatives. The AIRS-RTA can compute 12 complete AIRS spectra of all 2378 channels in one second using a commodity CPU circa 2001.

III. SPECTROSCOPY

This section provides a brief overview of the spectroscopy and line-by-line algorithms used in the AIRS-RTA. The spectroscopy determines the absolute accuracy of the AIRS-RTA. A reasonable lower limit on desired errors in the AIRS-RTA is the nominal noise level of 0.2 K, although some retrieval/assimilation schemes might require even lower biases relative to
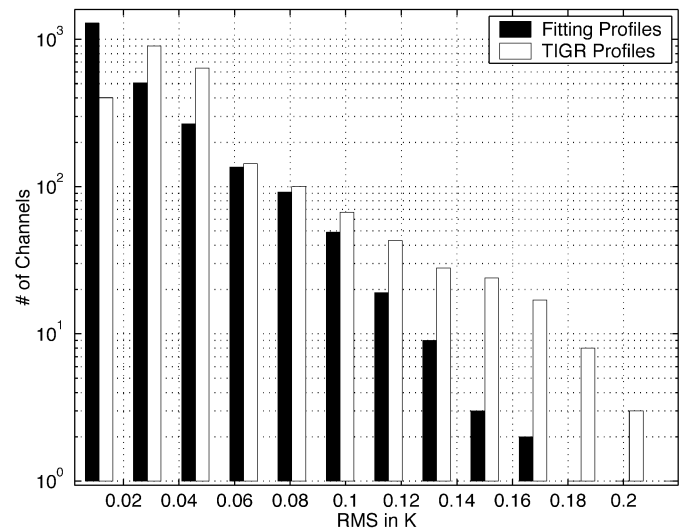
a model atmosphere. If the spectroscopic errors are systematic in each atmospheric layer (same percentage error) this translates into a maximum error of 1% in the spectroscopy. This is a demanding requirement, since it is often difficult to obtain agreement among different laboratory measurements of molecular line strengths to better than 2%, and even more difficult to measure line shapes to this accuracy.

The AIRS high-spectral resolution is most important in that it allows the use of channels in-between spectral lines, which have absorption coefficients proportional to pressure squared, that produce sharp weighting functions compared to channels on top of spectral lines. AIRS is therefore quite sensitive to the atmospheric spectral line shapes, especially for CO_2 and H_2O lines that have very high optical depths in the atmosphere. We summarize here the results of the development of improved CO_2 spectral line shapes, based on laboratory studies of CO_2 spectra that are in-turn validated with atmospheric emission spectra measured by the NAST-I and S-HIS high-spectral resolution interferometer radiometers flying on NASA's ER-2. Studies of H_2O line shapes are continuing, but uncertainties in the measurement of H_2O amounts in both the laboratory setting and in the atmosphere have slowed progress in H_2O line shapes, although extensive field campaigns by the DOE ARM [16] program should bear fruit in the near future.

One major consideration for CO_2 line shapes in the AIRS-RTA is the effect of line-mixing, which redistributes the radiation of overlapping spectral lines away from what would be computed using noninteracting Lorentz line shapes. Line-mixing reduces the effective far-wings of these interacting lines, while increasing the line shape near the line centers. Duration-of-collision effects also considerably reduce the CO_2 line wing from Lorentz values and is especially important in the head of the ν_3 band near 2400 cm^{-1} (4.3 μm) that contains excellent temperature sounding channels. The large effect of Q-branch line-mixing on high-spectral resolution nadir sounders was reported by Strow *et al.* [17] some years ago and has been reviewed more recently [18]. A number of popular line-by-line radiative transfer algorithms (GENLN2 and LBLRTM) incorporate Q-branch line mixing.

Line mixing in CO_2 P/R-branches has received less attention than Q-branch line-mixing because the P/R lines are more widely separated than Q-branch lines and it was believed that P/R mixing has less of an effect on the CO_2 spectrum. In addition, early studies ascribed the strong sub-Lorentz behavior of the ν_3 R-branch bandhead of CO_2 at 4.3 μm solely to duration-of-collision effects and neglected the strong influence of P/R-branch line-mixing. GENLN2 [19], for example, models the sub-Lorentz behavior of the CO_2 lines with the empirical model of Cousin *et al.* [20], which contains 14 line shape parameters, derived from laboratory spectra, to describe the ν_3 spectral line shapes. Subsequently, Cousin [21] and Boissoles [22] showed the P/R-branch line-mixing was responsible for much of the sub-Lorentz behavior of the R-branch bandhead, but their proposed model was too inaccurate for remote sensing applications.

The CO_2 line shape model for P/R-branch mixing and duration-of-collision effects used in the AIRS-RTA was developed by Tobin [23] and has been refined more recently by Machado *et al.* [24]. Tobin used laboratory spectra provided by John Johns [25] to develop an approximation for the combined effects of P/R-branch line-mixing and duration-of-collision effects that was physically based, had as few adjustable parameters as possible, and was sufficiently accurate for atmospheric remote sensing applications. This theory uses the same energy-gap scaling theory for rotational relaxation that has been successful in Q-branch studies, and adds a two-parameter adjustment for duration-of-collision effects that follows the approach of Birnbaum [26], [27]. He was able to accurately model both room and low-temperature CO_2 spectra in the R-branch band head with only three adjustable parameters, two parameterizing duration-of-collision effects, and one that scales the rotational relaxation that determines line-mixing.

P/R-branch line-mixing and duration-of-collision effects should also affect CO_2 line shapes in the strong 15-μm bands that are used for atmospheric temperature sounding. Duration-of-collision effects should be identical to what we observed in the ν_3 band. However, at 15 μm these effects are harder to observe because the various CO_2 bands in this region are more spread apart than in the 4-μm region. We expect P/R-branch line-mixing to be approximately half as strong in the 15-μm bands than in the 4.3-μm bands. The 4.3-μm bands are primarily $\Sigma - \Sigma$ bands that only have even, or odd, rotational levels present. The 15-μm bands of CO_2 are primarily $\Pi - \Sigma$ type bands which have *all* rotational levels present in the Π states. The end result is that half of the rotationally inelastic molecular collisions transfer the molecule to rotational states that are not connected to a radiative transition, and thus these collisions do not contribute to line mixing. This is in contrast to the situation in $\Sigma - \Sigma$ bands where all rotational states are connected to a radiative transition, so all rotationally inelastic collisions can lead to line mixing.

Our 15-μm CO_2 line shape uses the duration-of-collision parameters derived from CO_2 spectra at 4.3 μm, but computes line-mixing appropriate for $\Pi - \Sigma$ and $\Pi - \Delta$ bands. We use an energy-gap scaling law for the rotational relaxation that is parameterized by ensuring that the scaling law reproduces the observed linewidths as a function of J, the rotational state quantum
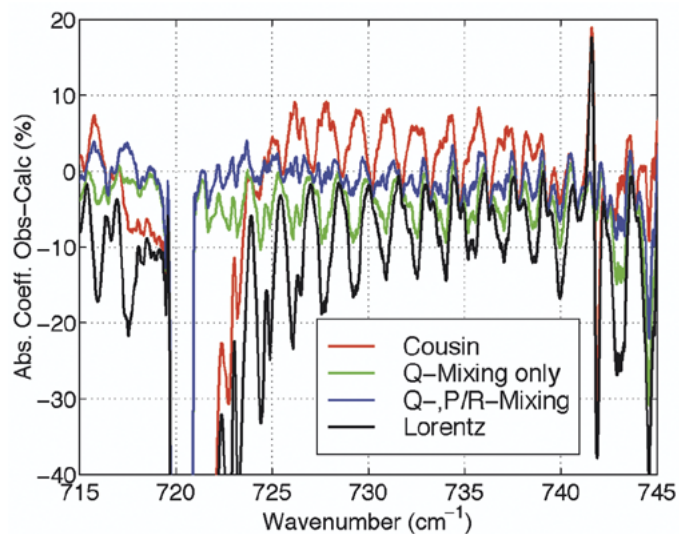

Fig. 5. Laboratory spectrum of CO_2 in the 15-μm region and percent errors in the computed absorption coefficients for this spectrum. This spectrum was 766 torr of CO_2, 15-cm path length, at 296.7 K.

number. Details of these calculations, and comparisons to laboratory data, can be found in [23] and [24]. Other line-by-line algorithms use various approximations for the far-wing CO_2 line shape. GENLN2, for example, uses the empirical Cousin [20] far-wing line shape for the CO_2 line shape, both at 4.3 and 15 μm, although Cousin derived the empirical parameters for this line shape using 4.3-μm spectra. Consequently, GENLN2 overestimates the effect of line-mixing at 15 μm, since it uses a $\Sigma - \Sigma$ parameterization to model the $\Pi - \Sigma$ band line wings at 15 μm.

Fig. 5 shows our observed minus computed absorption coefficients for a laboratory spectrum of CO_2 in the 15-μm region. The theory summarized above is labeled Q-, P/R-Mixing in this figure, which also shows results for the Cousin line shape, the standard Lorentz line shape, and a line shape that uses Q-branch mixing with Lorentz for the P/R-branch lines of the strong bands. The center of the strong Q-branch at 720 cm^{-1} is not well-modeled in any of these cases because the transmittance spectrum used for this figure was saturated in that region. Our line shape model calculation in this figure *used no adjustable parameters.* The duration-of-collision parameters from the 4.3-μm band were used, along with a standard computation of line-mixing that used a single parameter derived from Q-branch spectra that is constant for all bands with Q-branches. This result indicates that line-by-line codes using the Cousin line shape at 15 μm will overestimate line-mixing (computed brightness temperatures will be too large in a region with a positive lapse rate).

A. Validation With Aircraft Observations

Figs. 6 and 7 show comparisons between computed and observed brightness temperature spectra in the 15-μm region for the WINTEX (Winter EXperiment) and the CLAMS (Chesapeake Lighthouse and Aircraft Measurements for Satellites) aircraft campaigns. The WINTEX observations were made with the NPOESS/NASA-Langley NAST-I interferometer flying on NASA's ER-2 during March 1999. Atmospheric conditions in the vicinity of a colocated radiosonde launch during this flight
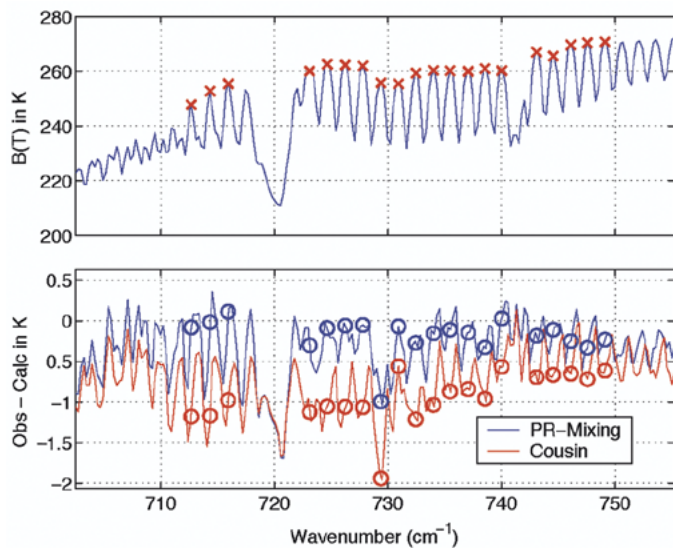
Fig. 6.   Observed minus computed spectrum in the longwave CO_2 bands. Observed spectrum taken by NAST-I on NASA's ER-2 during the WINTEX field campaign. The computed spectrum used the profile from a colocated radiosonde. The $\times$ markers in the top panel denote channels in between spectral lines, and the same channels are denoted with circles in the bottom panel.
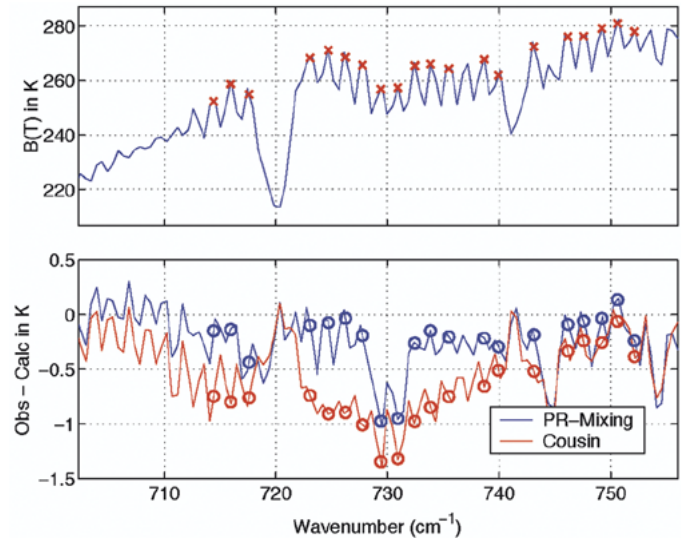

Fig. 7.   Observed minus computed spectra (mean errors shown). Observed spectra recorded by the Scanning-HIS spectrometer on the ER-2 during the CLAMS campaign. The computed spectra used ECMWF forecast/analysis fields for the profiles. The $\times$ markers in the top panel denote channels in between spectral lines, and the same channels are denoted with circles in the bottom panel.

were very uniform and largely clear. The computed spectra used the radiosonde (CLASS sonde) profile and line-by-line calculations of the radiance, one using our P/R-Mixing algorithm and the other using the Cousin parameterization for the CO_2 line shape.

The CLAMS measurements were made with the University of Wisconsin's Scanning-HIS interferometer, aboard the ER-2 on July 17, 2001 off the coast of Wallops Island, VA, under nominally clear conditions. The CLAMS calculations used the ECMWF (European Centre for Medium-Range Weather Forecasts) forecast/analysis model fields for the profile. The Scanning-HIS flew a regular flight pattern that covered 11 ECMWF $0.5°$ grid cells. The calculations shown in the bottom of Fig. 7 are the biases for approximately 3500 individual fields of view covering the 11 ECMWF grid cells. These 3500 points represent 77% of the Scanning-HIS observations. The remaining 23% of the observations were discarded because of cloud/land contamination. In addition, the computed sea-surface temperature was adjusted by approximately $0.5°$ to obtain agreement between observed and computed mean sea-surface temperature (window channels). This adjustment ensures that the observed minus computed plot emphasizes errors in the atmospheric transmittances.

Both Figs. 6 and 7 exhibit the same general error in the Cousin line shape in the 710–740-cm^{-1} region. Although these differences are relatively small, they are 5–10 times greater than the AIRS accuracy requirements. It is also encouraging that we see the same improvements in the observed minus computed radiances using different instruments (NAST-I, S-HIS) and different sources for the atmospheric profile (radiosondes, ECMWF model data). The more irregular structures in these observed minus computed spectra are either due to an inadequate temperature profile at higher altitudes, or due to water vapor lines that are in error either due to the spectroscopy, or more likely, due to uncertainties in the water vapor profile. We

expect higher errors at line centers where much of the atmospheric emission originates high in the atmosphere near the aircraft. The radiosonde errors may be larger at these high altitudes ($\sim$50 hPa), contributing some of the observed differences in the WINTEX case. In addition, neither the radiosonde nor the ECMWF profiles are appropriate for the temperature profile very close to the aircraft where the air path temperature is probably modified by the local aircraft environment. The good agreement between observed and computed brightness temperatures near $720\ cm^{-1}$ in the CLAMS case is surprising, and possibly fortuitous, since this emission also originates close to the plane.

Fig. 8 is the WINTEX spectrum shown earlier, but now in the 4.3-μm temperature sounding region where line-mixing is very strong. Again, the calculations were done for both the Cousin line shape and our P/R-branch line shape. The better agreement for our P/R-branch calculation is attributed to better laboratory data that was used to compute the three adjustable parameters (two for duration-of-collision and one for line-mixing) and to our more physically based treatment of line-mixing and duration-of-collision effects inside the band. Similar differences between these two line shapes have been seen in other aircraft spectra.

Finally, we show observed minus computed spectra in the water vapor region, Fig. 9. The bottom panel in this plot shows observed minus computed spectra for the WINTEX spectrum discussed earlier, and for a clear-sky spectrum taken by the HIS interferometer on the ER-2 during the CAMEX-1 (Convection and Moisture EXperiment) in 1993. Both spectra were computed using a colocated radiosonde profile. The key feature of these calculations is the relatively good agreement in-between spectral lines (lower altitude water) and the poor, and variable, agreement on top of spectral lines (high-altitude water). Errors in-between lines of $\sim$2 K near $1600\ cm^{-1}$ are a consequence of changes to CKD 2.4, the water vapor continuum,
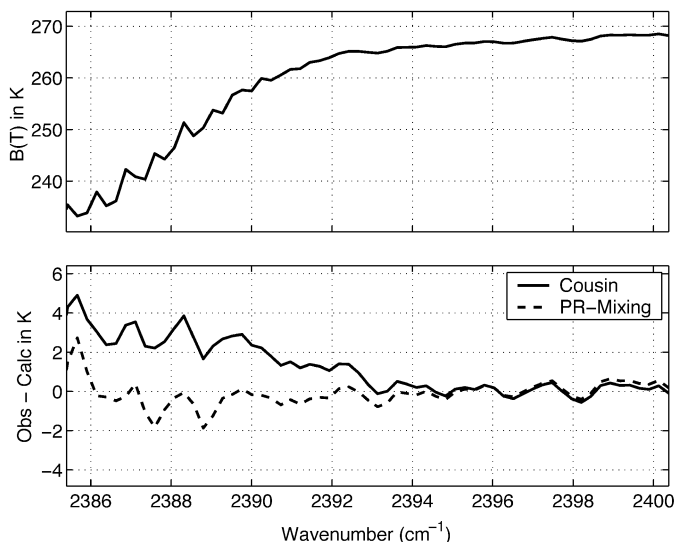
Fig. 8. Observed minus computed spectrum around the shortwave CO_2 Ft. sounding channels. Observed spectrum taken by NAST-I on NASA's ER-2 during the WINTEX field campaign. The computed spectrum used the profile from a colocated radiosonde.
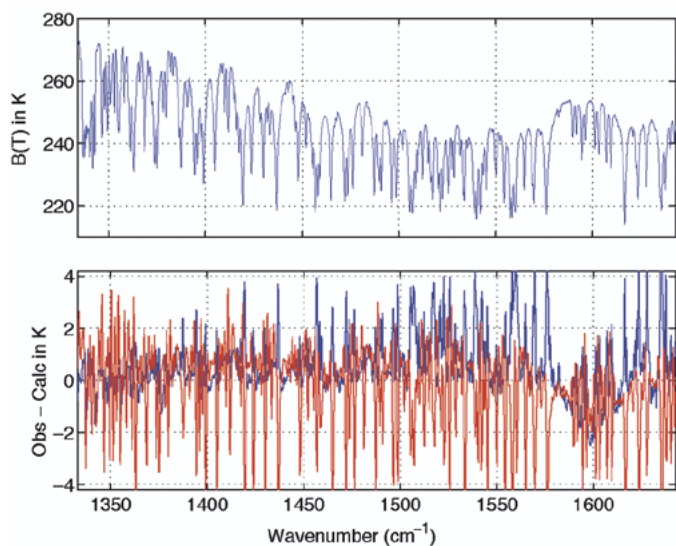

Fig. 9. Observed minus computed spectrum in wavenumber regions dominated by water vapor. (Top) Observed spectrum taken by NAST-I on NASA's ER-2 during the WINTEX field campaign. (Bottom) Observed minus computed spectra for the WINTEX spectrum shown above (blue) and for a spectrum taken during the CAMEX-1 campaign (red).

from earlier versions. If CKD 2.3 is used instead, the errors near 1600 cm^{-1} are reduced by more than 1 K. Comparisons between the CAMEX-1 spectrum and a water vapor continuum developed by Strow *et al.* [28] show even better agreement in this spectral region. The AIRS-RTA discussed here uses CKD 2.4, but later versions will use a new continuum based on CKD 2.4, combined with the results of [28] and the analysis of AIRS validation data.

We expect the radiative transfer calculations on top of lines to be more accurate than calculations between lines, since the calculations between lines are dominated by the water vapor continuum, which is always difficult to measure in the laboratory
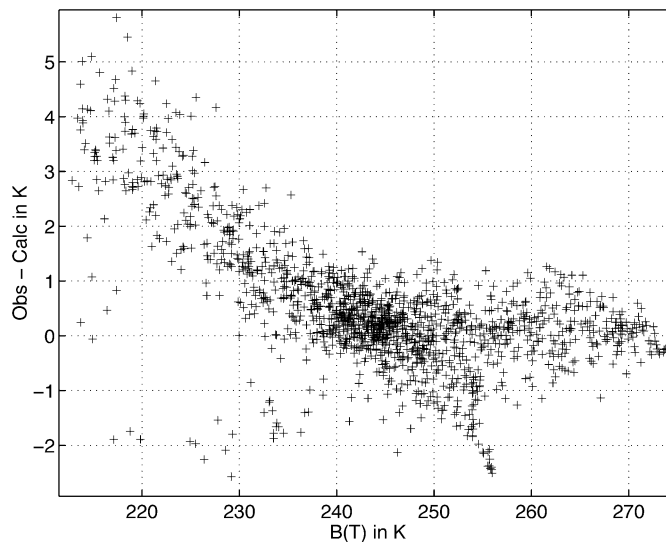

Fig. 10. Observed minus computed brightness temperatures shown in Fig. 9, but plotted against the computed water vapor brightness temperature. This plot shows that the obs-calc errors are smaller for the higher temperature (lower altitude) channels where the radiosonde profile is expected to be more accurate.

relative to the water vapor line strengths and widths. We therefore attribute the poor agreement on top of lines to uncertainties in the sonde water vapor profiles at high altitudes, which are commonly acknowledged to contain high errors.

Fig. 10 is a scatter plot of the observed minus computed brightness temperatures versus the computed brightness temperature for the WINTEX case. This plot emphasizes that most of the differences between observed and computed spectra are at the lower temperatures, although there are significant differences at the band center near 1600 cm^{-1} that are several Kelvin, which as stated above are significantly reduced using CKD 2.3 instead of CKD 2.4.

B. kCARTA and UMBC-LBL

The monochromatic atmospheric transmittances that form the core of the AIRS-RTA are computed using the kCARTA line-by-line algorithm [12], [13]. kCARTA computes transmittances and/or radiances from compressed lookup tables of atmospheric transmittances, resulting in very fast computation times. kCARTA is an extensively documented [13] FORTRAN 77 program that is available from the authors. The compressed lookup tables that accompany kCARTA require ∼600 MB of storage space.

The kCARTA lookup table transmittances were computed with a custom line-by-line (LBL) algorithm developed by the authors, which we call UMBC-LBL. The only real requirement on the UMBC-LBL is to compute kCARTA's static lookup tables of compressed transmittances. These tables only change when improvements are made to the molecular line parameters or gas cross-sections, an infrequent occurrence. Since speed is not an important issue for UMBC-LBL we can accurately model both Q-, and P/R-branch mixing in UMBC-LBL, and not rely on perturbation solutions. At present UMBC-LBL includes CO_2 line-mixing for 12 Q-branch and 12 P/R-branch bands. The P/R-

branch bands also include a duration-of-collision term discussed earlier. A detailed description of UMBC-LBL is available [29].

IV. SUMMARY

This paper provides an overview of the AIRS radiative transfer algorithm, covering both the spectroscopy and the fast parameterization of the radiative transfer used in the retrieval of atmospheric profiles from AIRS observed radiances. In addition, we have presented summaries of the results of field experiments using aircraft observations of high-spectral resolution radiances that validate the spectroscopy used in the AIRS-RTA. These results suggest that the AIRS-RTA has accuracies approaching the 0.2 K level for channels dominated by CO_2. Accuracies of the AIRS-RTA for water vapor channels are more difficult to ascertain, although in-between spectral lines field measurements suggest errors on the order of 1 K or better in most spectral regions. RTA accuracies for higher altitude water channels (line centers) are difficult to validate with aircraft measurements. However, the spectroscopy relevant to radiative transfer at the centers of water lines should be quite accurate, since these parameters are relatively easy to measure in the laboratory, and have been studied extensively in the last several years.

The results of the work presented here are available from the authors in the form of two packages: 1) a version of the AIRS-RTA (fast model) [10] that can operate outside of the AIRS retrieval system; and 2) the kCARTA pseudo line-by-line radiative transfer algorithm [13].

The AIRS validation effort [30] will provide a number of opportunities for validation of the AIRS-RTA, although reaching the 0.2K level of accuracy will always be challenging.

ACKNOWLEDGMENT

REFERENCES

[1] H. H. Aumann, M. T. Chahine, C. Gautier, M. D. Goldberg, E. Kalnay, L. M. McMillin, H. Revercomb, P. W. Rosenkranz, W. L. Smith, D. H. Staelin, L. L. Strow, and J. Susskind, "AIRS/AMSU/HSB on the Aqua mission: Design, science objectives, data products, and processing systems," *IEEE Trans. Geosci. Remote Sensing*, vol. 41, pp. 253–264, Feb. 2003.

[2] S. E. Hannon and L. L. Strow, "The AIRS radiative transfer algorithm,", to be published.

[3] L. L. Strow, S. E. Hannon, M. Weiler, K. Overoye, S. L. Gaiser, and H. H. Aumann, "Prelaunch spectral calibration of the Atmospheric Infrared Sounder (AIRS)," *IEEE Trans. Geosci. Remote Sensing*, vol. 41, pp. 274–286, Feb. 2003.

[4] M. Geller, "A high-resolution atlas of the infrared spectrum of the Sun and the Earth atmosphere from space: Key to identification of solar features," NASA, Tech. Rep. NASA Ref. Pub. 1224, vol. III, 1992.

[5] J. Susskind, J. Rosenfield, and D. Reuter, "An accurate radiative transfer model for use in the direct physical inversion of HIRS 2 and MSU temperature sounding data," *J. Geophys. Res.*, vol. 88, no. C13, pp. 8550–8568, 1983.

[6] J. Kornfield and J. Susskind, "On the effect of surface emissivity on temperature retrievals," *Mon. Weather Rev.*, vol. 105, pp. 1605–1608, 1977.

[7] L. M. McMillin, L. J. Crone, M. D. Goldberg, and T. J. Kleespies, "Atmospheric transmittance of an absorbing gas 4:OPTRAN: A computationally fast and accurate transmittance model for absorbing gases with fixed and variable mixing ratios at variable viewing angles," *Appl. Opt.*, vol. 34, pp. 6269–6274, 1995.

[8] L. M. McMillin, L. J. Crone, and T. J. Kleespies, "Atmospheric transmittance of an absorbing gas 5: Improvements to the OPTRAN approach," *Appl. Opt.*, vol. 34, pp. 8396–8399, 1995.

[9] S. Hannon, L. L. Strow, and W. W. McMillan, "Atmospheric infrared fast transmittance models: A comparison of two approaches," in *Proc. SPIE Conf. 2830, Optical Spectroscopic Tech. Instrument. Atmospher. Space Res. II*, 1996.

[10] S. E. Hannon and L. L. Strow. (2002) SARTA: The standalone airs radiative transfer algorithm. Univ. Maryland Baltimore County, Dept. Physics, Tech. Rep. [Online]. Available: http://asl.umbc.edu/pub/rta/sarta.

[11] V. Achard, "Trois problemes cles de l'analyze 3D de la structure thermodinamique de l'atmosphere par satellite: Mesure du contenu en ozone: classification des masses d'air; modelization hyper rapide du ransfert radiatif," Ph.D. dissertation, LMD, Ecole Polytechnique, Palaiseau, France, 1991.

[12] L. L. Strow, H. E. Motteler, R. G. Benson, S. E. Hannon, and S. De Souza-Machado, "Fast computation of monochromatic infrared atmospheric transmittances using compressed look-up tables," *J. Quant. Spectrosc. Rad. Trans.*, vol. 59, no. 3–5, pp. 481–493, 1998.

[13] S. De Souza-Machado, L. L. Strow, H. E. Motteler, and S. E. Hannon. (2002) kCARTA: An atmospheric radiative transfer algorithm using compressed lookup tables. Univ. Maryland Baltimore County, Dept. Physics, Tech. Rep. [Online]. Available: http://asl.umbc.edu/pub/rta/kcarta.

[14] L. S. Rothman, C. P. Rinsland, A. Goldman, S. T. Massie, D. P. Edwards, J. M. Flaud, A. Perrin, C. Camy-Peyret, V. Dana, J. Y. Mandin, J. Schroeder, A. McCann, R. R. Gamache, R. B. Wattson, K. Yoshino, K. V. Chance, K. W. Jucks, L. R. Brown, V. Nemtchinov, and P. Varanasi, "The HITRAN molecular spectroscopic database and HAWKS (HITRAN atmospheric workstation): 1996 edition," *J. Quant. Spectrosc. Rad. Trans.*, vol. 60, pp. 665–710, 1998.

[15] J. Susskind, C. D. Barnet, and J. M. Blaisdell, "Retrieval of atmospheric and surface parameters from AIRS/AMSU/HSB data in the presence of clouds," *IEEE Trans. Geosci. Remote Sensing*, vol. 41, pp. 390–409, Feb. 2003.

[16] G. M. Stokes and S. E. Schwartz, "The Atmospheric Radiation Measurement (ARM) Program programmatic background and design of the cloud and radiation testbed," *Bull. Amer. Meteorol. Soc.*, vol. 75, pp. 1201–1221, 1994.

[17] L. L. Strow and D. Reuter, "Effect of line mixing on atmospheric brightness temperatures near 15 μm," *Appl. Opt.*, vol. 27, p. 872, 1988.

[18] L. L. Strow, "CO_2 Q-branch spectral line shapes for atmospheric remote sensing," in *High Spectral Resolution Infrared Remote Sensing for Earth's Weather and Climate Studies*, A. Chedin, M. T. Chahine, and N. A. Scott, Eds. New York: Springer-Verlag, 1993, pp. 459–475.

[19] D. P. Edwards, "Genln2: A general line-by-line atmospheric transmittance and radiance model," National Center for Atmospheric Research, Boulder, CO, NCAR Tech. Note 367+STR, 1992.

[20] C. Cousin, R. Le Doucen, C. Boulet, and A. Henry, "Temperature dependence of the absorption in the region beyond the 4.3μm band head of CO_2: 2: N_2 and O_2 broadening," *Appl. Opt.*, vol. 24, p. 3899, 1985.

[21] C. Cousin, R. Le Doucen, C. Boulet, A. Henry, and D. Robert, "Line coupling in the temperature and frequency dependencies of absorption in the microwindows of the 4.3μm CO_2 band," *J. Quant. Spectrosc. Rad. Trans.*, vol. 36, p. 521, 1986.

[22] J. Boissoles, C. Boulet, L. Bonamy, and D. Robert, "Calculation of absorption in the microwindows of the 4.3μm CO_2 band from an ECS scaling analysis," *J. Quant. Spectrosc. Rad. Trans.*, vol. 42, p. 509, 1989.

[23] D. C. Tobin, "Infrared spectral lineshapes of water vapor and carbon dioxide," Ph.D. dissertation, Univ. Maryland Baltimore County, Baltimore, MD, 1996.

[24] S. De Souza-Machado, L. L. Strow, D. Tobin, H. Motteler, and S. E. Hannon, "Improved atmospheric radiance calculations using CO_2 p/r-branch line mixing," in *Proc. Euro. Symp. Aerospace Remote Sensing Europto Series*, Sept. 1999.

[25] J. W. C. Johns, "Private communication: μm CO_2 spectra," unpublished, 1992.

[26] G. Birnbaum and E. R. Cohen, "Theory of line shape on pressure-induced absorption," *Can. J. Phys.*, vol. 54, p. 593, 1976.

[27] G. Birnbaum, "The shape of collision broadened lines from resonance to the far wings," *J. Quant. Spectrosc. Radiat. Transfer*, vol. 21, pp. 597–607, 1979.

[28] L. L. Strow, D. C. Tobin, W. W. McMillan, S. E. Hannon, W. L. Smith, H. E. Revercomb, and R. Knuteson, "Impact of a new water vapor continuum and line shape model on observed high resolution infrared radiances," *J. Quant. Spectrosc. Rad. Trans.*, vol. 59, no. 3–5, pp. 303–317, 1997.

[29] S. De Souza-Machado, L. L. Strow, D. Tobin, H. E. Motteler, and S. E. Hannon. (2002) UMBC-LBL: An algorithm to compute line-by-line spectra. Univ. Maryland Baltimore County, Dept. Physics, Tech. Rep. [Online]. Available: http://asl.umbc.edu/pub/rta/umbclbl.

[30] E. Fetzer, L. M. McMillin, D. Tobin, H. H. Aumann, M. R. Gunson, W. W. McMillan, D. E. Hagan, M. D. Hofstadter, J. Yoe, D. N. Whiteman, J. E. Barnes, R. Bennartz, H. Vomel, V. Walden, M. Newchurch, P. J. Minnett, R. Atlas, F. Schmidlin, E. T. Olsen, M. D. Goldberg, S. Zhou, H. Ding, W. L. Smith, and H. Revercomb, "AIRS/AMSU/HSB validation," *IEEE Trans. Geosci. Remote Sensing*, vol. 41, pp. 418–431, Feb. 2003.

Sergio De Souza-Machado received the B.S. degree in math/physics from the College of Wooster, Wooster, OH, in 1988, and the M.S. and Ph.D. degrees in physics from the University of Maryland, College Park, in 1990 and 1996, respectively.

He is currently an Assistant Research Scientist with the Department of Physics, University of Maryland—Baltimore County, Baltimore. His research interests include atmospheric physics, focusing on radiative transfer and molecular spectroscopy, as well as plasma physics.

L. Larrabee Strow received the B.S. degree in physics from the University of Maryland—Baltimore County (UMBC), Baltimore, in 1974, and the M.S. and Ph.D. degrees in physics from the University of Maryland, College Park, in 1977 and 1981, respectively.

He is currently a Professor with the Department of Physics, UMBC. His research interests include molecular spectroscopy, especially spectral line shapes, and atmospheric remote sensing. He is a member of the AIRS Science Team.

Howard E. Motteler (M'88) received the B.S. degree in mathematics from the University of Puget Sound, Tacoma, WA, in 1980, the M.S. degree in computer science from Purdue University, West Lafayette, IN, in 1982, and the Ph.D. degree in computer science from the University of Maryland, College Park, in 1987.

He is currently a Research Associate Professor at Joint Center for Earth Systems Technology, University of Maryland—Baltimore County (UMBC), Baltimore, while remaining affiliated with the UMBC's CSEE Department. His current research interests are in the areas of scientific computation and applications in atmospheric science, including passive infrared and microwave sounding and radiative transfer calculations.

Scott E. Hannon received the B.A. and M.S. degrees from the University of Maryland—Baltimore County (UMBC), Baltimore, in 1986 and 1990, respectively, all in physics.

Since then, he has been with the UMBC working on topics related to atmospheric physics, with a focus on the development of a fast-forward model for the AIRS instrument.

David Tobin received the B.S., M.S., and Ph.D. degrees from the University of Maryland—Baltimore County, Baltimore, in 1991, 1993, and 1996, respectively, all in physics.

He is currently a Researcher at the Cooperative Institute for Meteorological Satellite Studies, Space Science and Engineering Center, University of Wisconsin, Madison. His current research includes involvement with ground-, aircraft-, and satellite-based FTIR programs, the Atmospheric Radiation Measurements program, and the Atmospheric Infrared Sounder.